Screened-exchange determination of the electronic properties of monoclinic, tetragonal, and cubic zirconia

J. E. Medvedeva*
Department of Physics, Missouri University of Science and Technology, Rolla, Missouri 65409, USA

A. J. Freeman
Department of Physics and Astronomy, Northwestern University, Evanston, Illinois 60208, USA

C. B. Geller and D. M. Rishel
Bechtel Bettis Laboratory, West Mifflin, Pennsylvania 15122, USA

(Received 11 May 2007; revised manuscript received 9 August 2007; published 13 December 2007)

First-principles electronic band structure investigations of monoclinic, tetragonal, and cubic ZrO_2 reveal the highly anisotropic nature of the conduction and valence band topologies in the monoclinic phase with electron and hole effective masses differing by over an order of magnitude in perpendicular directions. The planes of relatively high implied electron and hole mobilities intersect along a single crystallographic direction, making this the only direction readily available for exciton motion. Conversely, in the tetragonal and cubic phases, charge carrier effective masses are more isotropic and exciton motion is less restricted. These findings may explain recent experimental observations suggesting that exciton production via gamma irradiation in zirconia crystallites immersed in water is responsible for the accelerated dissociation of adsorbed water molecules on crystallite surfaces, and for the specificity of the effect to the tetragonal zirconia phase.

DOI: 10.1103/PhysRevB.76.235115 PACS number(s): 71.20.−b

INTRODUCTION

Zirconium based alloys, such as the Zircaloys, have long been the cladding materials of choice for pressurized water reactor fuel elements, by virtue of zirconium's low thermal neutron capture cross section and resonance integral, its relatively high melting temperature, and its favorable aqueous corrosion resistance. Thus, radiation effects on zirconium alloy aqueous corrosion have been a subject of long standing interest in the nuclear industry. The key to good aqueous corrosion resistance in the zirconium alloys is the passive, protective nature of the dense, adherent oxide scale that develops in water on exposed alloy surfaces. Long-term corrosion rates are determined by mechanical and crystallographic instabilities of aqueous corrosion films.[1] Aqueous high-temperature corrosion of Zircaloy normally results in the formation of a uniform oxide layer that initially grows in thickness at a rate proportional to the one-third power of time. Such corrosion films undergo mechanical and crystallographic instabilities at thicknesses of about 2–3 μm, leading to accelerated corrosion kinetics. This kinetics change is referred to as transition. Post-transition films are observed to consist of parallel layers of dense oxide separated by thin strata containing many "submicron" sized pores and/or cracks.[2,3]

In the post-transition corrosion regime, oxide growth typically exhibits linear kinetics. Mechanistically, this behavior is interpreted to be either the result of repeated local pretransition cycles that grow progressively out of phase on different parts of the corroding surface or due to counterbalancing growth and breakdown mechanisms in the scale resulting in a protective layer of constant thickness. In the latter interpretation, the thickness of the protective portion of the oxide scale is thought to be limited either by zirconia crystallographic phase instabilities in the strained, impure zirconia or by porosity percolation. In both interpretations, the innermost oxide layer, i.e., the barrier layer, is believed to limit mass or charge transport.

Except for the region directly adjacent to the metal-oxide interface, most of the thickness of such films is thought to consist of parallel columns of primarily monoclinic oxide separated by vertical networks of nanometer sized pores that are much smaller than those found on the horizontal layer boundaries. *In situ*, the vertical pore networks are believed to be permeated by water (or steam), so that at most only a relatively thin layer of oxide adjacent to the metal/oxide interface prevents direct access by water to the metal substrate. The oxide forms entirely by the inward diffusion of oxygen. Thus, as a result of the high Pilling-Bedworth ratio (the ratio of the oxide volume to the volume of the metal from which it formed) of 1.56, the oxide scale directly adjacent to the metal substrate is in a high state of biaxial compression. A variety of experimental investigations via transmission electron microscopy,[4–8] Raman spectroscopy,[9] and x-ray diffraction studies[10] confirm that the key protective region of oxide near this interface consists of a combination of monoclinic, tetragonal, and sometimes amorphous components. The apparent low-temperature metastability of the tetragonal oxide polymorph near the metal-oxide interface may be attributed to compressive stress and perhaps other factors. For instance, nanosize grains may stabilize a nonequilibrium phase via surface energy considerations.

Petrik *et al.*[11] have reported that of 30 different oxide materials that were subject to γ irradiation, only those oxides with fundamental electronic band gap values between 4.5 and 6 eV, including zirconia, exhibited increased rates of adsorbed water dissociation. Citing this "resonant" behavior, they attributed the increase in the observed water dissocia-

tion rate to γ-induced exciton formation within those materials with a band gap value close to but greater than the O-H bond dissociation energy in adsorbed water. Separately, LaVerne[12] reported on the formation of H_2 in the radiolysis of liquid water containing nanometer sized ZrO_2 particles and found the evolution rate of H_2 to depend on the crystalline structure of the particles. Radiolysis of liquid water containing tetragonal ZrO_2 particles exhibits a significant increase in the rate of decomposition of water to H_2 compared with water containing only monoclinic zirconia particles or water alone. Annealing the tetragonal particles to the monoclinic structure eliminated excess H_2 production above that found with water alone.

While the electronic band structure of the monoclinic, tetragonal, and cubic phases of pure zirconia has been a subject of numerous studies,[13–22] here we show that nonlocal corrections to the local density approximation (LDA), such as in the screened exchange LDA, are crucial for accurate determination of the band gaps and the valence and/or conduction band topology of the zirconia phases. Moreover, detailed comparison of the screened exchange local density approximation (sX-LDA) calculated electron and hole effective masses of the monoclinic, tetragonal, and cubic phases helps elucidate their different radiolytic behavior under γ radiation.

APPROACH

The electronic band structure calculations of monoclinic (m), tetragonal (t), and cubic (c) zirconia were performed using the highly precise all-electron full-potential linearized augmented plane-wave method.[23] In order to determine accurately the fundamental band gap value and the valence and/or conduction band topology for each zirconia phase, we employed the self-consistent sX-LDA[24–28] which provides a better energy functional beyond the LDA or generalized gradient approximation by modeling the exchange-correlation hole within a *nonlocal* density scheme. In contrast to the GW approximation, which also removes most of the problems of LDA in treating excitation properties by calculating the self-energy in terms of the single particle Green function G and the screened interaction W, the sX-LDA is much less computationally demanding and it also enables the self-consistent determination of the ground state and excited state properties. The screened nonlocal exchange Hamiltonian is similar in spirit to various hybrid functional approaches with two principal differences: (i) The relative weight of the LDA and nonlocal exchange contributions is dictated by the specific physical system being modeled, through the value of the valence electron Thomas-Fermi screening length, rather than being fixed *a priori* for all systems. We argue that this fact gives the sX-LDA method a more *ab initio* character than hybrid functional methods. (ii) The Thomas-Fermi screening function emphasizes the shorter range contributions of nonlocal exchange. The success of the sX-LDA in systematically improving the description of the excited states in various narrow-to-wide band gap (IV, III-V, and II-VI semiconductors, Bi_2Te_3, nitrides, and transparent conducting oxides) and insulating (CaF_2) materials has been recognized.[29–34] In this work, we apply the sX-LDA approach to a d^0 metal oxide, ZrO_2, and show that the nonlocal density scheme gives a significant improvement over LDA. In addition, using the second variation method,[35] spin-orbit coupling was included self-consistently. For the sX-LDA+SO calculations, cutoffs for the plane wave basis and the star functions were 17.6 Ry and 100 Ry, respectively, and all angular momentum contributions with $l \leqslant 8$ were included within the muffin-tin spheres. Zr $4p^6$ states and O $2s^2$ states, which were treated as valence, were excluded from screening. Summations over the Brillouin zone were carried out using at least ten special **k** points in the irreducible wedge; for each system, the convergence of absolute values of the total energy was checked carefully using finer k-point meshes. For each structure under consideration, both the lattice parameters and the internal coordinates of all atoms in the cell were optimized via total energy and atomic force minimization. Finally, our total energy calculations correctly predict the relative stability of the pure phases, namely, $m < t < c$, at zero temperature.

ELECTRONIC BAND STRUCTURE

First, we examine the electronic band structure of pure low-pressure zirconia in its cubic ($Fm\bar{3}m$), tetragonal ($P4_2/nmc$), and monoclinic ($P2_1/c$) phases. LDA and sX-LDA band structures are presented in Fig. 1. In agreement with previous calculations,[17–19,22] it is found for all three phases that the top of the valence band (VB) is formed from oxygen $2p$ states, whereas the bottom of the conduction band (CB) is formed from zirconium $4d$ states. As expected, the predicted width of the O $2p$ valence band decreases from the high- to the low-temperature phase in the order $c > t > m$, within both the LDA and sX-LDA. It is also found that in the tetragonal and cubic phases, but not the monoclinic, the unoccupied Zr $4d$ states at the bottom of the conduction band are split off from the rest of the CB; in these, the LDA (sX-LDA) gap values are 0.99 (0.92 eV) and 1.27 (1.02 eV), respectively, cf. Fig. 1.

In Table I, we compare the calculated LDA and sX-LDA direct and indirect band gaps for all three zirconia phases. As can be seen, use of the screened-exchange approximation results in a systematic increase of the LDA band gaps for all three systems. This shift is not rigid in the manner of a "scissors" operator but, rather, is found to depend on crystal momentum. The LDA predicts the largest indirect fundamental band gap value for tetragonal zirconia and the smallest for the cubic phase. This ordering agrees with previously reported LDA results.[19,22] However, the sX-LDA changes the order of the minimum band gap values among zirconia phases such that the monoclinic phase is predicted to have a slightly larger indirect gap than the tetragonal. This result is satisfying since the fundamental band gap, which is an energy splitting between bonding and antibonding states, is a secondary indicator of relative stability. Nevertheless, the largest optical (i.e., direct) sX-LDA band gap remains in the tetragonal phase. It is noted that for the tetragonal phase, the sX-LDA valence band maximum is found to be at the A point of the Brillouin zone. This prediction might appear to conflict with recent GW results,[19] where the maximum was re-

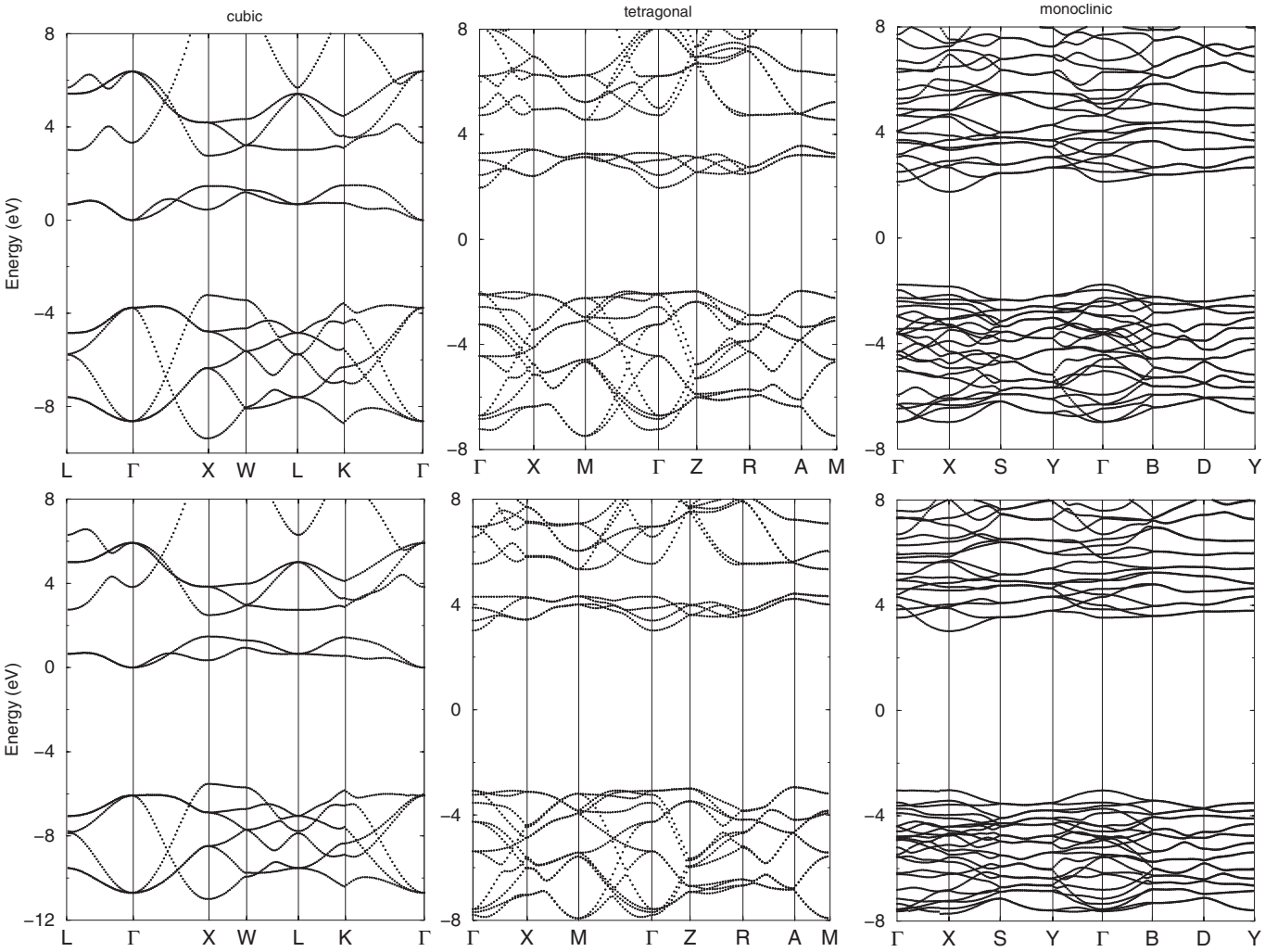

FIG. 1. LDA (top) and sX-LDA (bottom) band structures of the cubic, tetragonal, and monoclinic zirconia phases.

ported to lie between the Γ and *M* points, except that the *A* point was not reported in the GW band structure calculation. Finally, the sX-LDA calculated band gap for monoclinic zirconia falls within the large range of the available experimental values, from 4.2 up to 7.1 eV as measured by different techniques.[18,36–39] The spread among reported experimental values is considerably wider than the disagreement between experiments and sX-LDA band gap predictions previously reported, which is typically less than 10%.

The calculated zero-temperature sX-LDA direct band gap values of all three zirconia phases, which differ by at most 0.2 eV from one another, cf. Table I, allow the possibility of producing an exciton with sufficient energy to break an O-H bond in a water molecule (the energy of the H-OH bond is 5.1 eV). It should be noted here that above room temperature, the relevant band gap values for the zirconia phases are expected to be several tenths of an eV smaller than the calculated zero-temperature values, placing them all well inside the excitonic energy range of 4.5–6.0 eV for resonant water dissociations reported by Petrik *et al.*[11] The band gaps of the denser tetragonal and cubic phases are expected to show the greatest temperature dependence. The correlation seen by Petrik was with bulk. (We note here that changes in the band gap values at the surface may be more significant than the gap variations with temperature. Surface studies are beyond the scope of the present work.) However, the similarity of the band gap values for the monoclinic and tetragonal phases (6.04 and 5.95 eV, respectively) offers no insight, in and of itself, into their dissimilar heterogeneous radiolytic behavior.

TABLE I. Direct (indirect) zero-temperature band gap values, in eV, for monoclinic, tetragonal and cubic ZrO_2 calculated within LDA and sX-LDA.

	Monoclinic	Tetragonal	Cubic
LDA	3.59 (3.52)	4.03 (3.93)	3.67 (3.22)
sX-LDA	6.04 (6.05)	6.08 (5.95)	5.87 (5.53)

BAND TOPOLOGIES AND EFFECTIVE MASSES

To understand the differences in radiolytic properties of the monoclinic and tetragonal phases under γ radiation, we analyzed the conduction and valence band topologies of all three zirconia phases. First, we note that due to the relatively flat conduction and valence bands of the monoclinic phase,

TABLE II. Calculated sX-LDA (LDA) effective electron and hole band masses (in m_e) for the monoclinic, tetragonal, and cubic phases of ZrO_2 along the high-symmetry directions.

	Conduction band mass	Valence band mass
	Monoclinic phase	
ΓX [100]	1.067 (1.088)	−10.502 (−9.073)
ΓY [010]	1.134 (0.719)	−2.233 (−1.800)
ΓB [001]	9.555 (2.720)	−1.761 (−1.507)
	Tetragonal phase	
ΓX [010]	0.952 (0.674)	−1.895 (−3.704)
ΓM [110]	0.976 (0.667)	−1.883 (−1.587)
ΓZ [001]	2.127 (2.111)	−10.545 (−10.627)
ΓA [111]	1.000 (0.792)	−0.991 (−1.483)
	Cubic phase	
ΓX [010]	2.048 (2.046)	−0.353 (−0.293)
ΓL [111]	1.220 (0.828)	−1.389 (−0.950)
ΓK [110]	1.671 (1.384)	−0.283 (−0.213)
ΓW [120]	2.027 (1.867)	−0.710 (−0.599)

the band edge density of states values are high, such that the Fermi level (E_F) shifts by only 0.115 and 0.087 eV, respectively, even for the high n or p carrier concentrations of $\pm 7.5 \times 10^{20}$ cm^{-3}.[40] Further, in Table II, we compare the electron and hole effective masses calculated in several high-symmetry directions of the corresponding Brillouin zone. Large anisotropies in the effective masses are evident, especially in the monoclinic and tetragonal phases, suggesting similar anisotropies in carrier mobility. The conduction and valence band topologies for monoclinic zirconia, the most anisotropic phase, are illustrated in Figs. 2 and 3. These three-dimensional band structure plots are calculated for the specified plane in the Brillouin zone while the energy runs along the third direction, z. The planes of constant energy

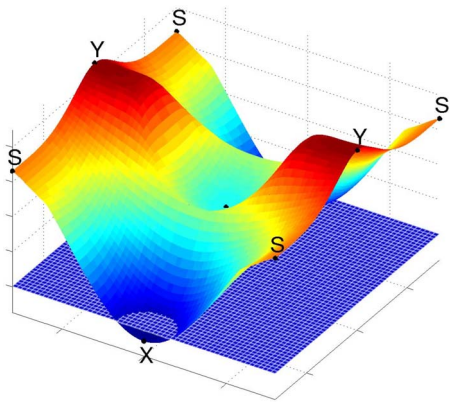

FIG. 2. (Color online) The anisotropic conduction band topology of monoclinic zirconia, showing where a carrier pocket would reside. The plane of constant energy corresponds to the electron concentration of 7.5×10^{20} cm^{-3}. The low effective mass and/or high mobility direction is from X to Γ.

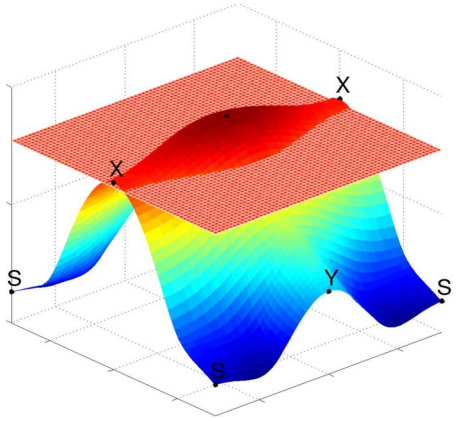

FIG. 3. (Color online) The valence band topology of monoclinic zirconia showing the location of the hole pocket that would be present in a doped, substoichiometric, or impure material. The plane of constant energy corresponds to the hole concentration of 7.5×10^{20} cm^{-3}. The low effective mass and/or high mobility direction runs from Γ to Y.

which show the electron or hole pockets correspond to the carrier concentrations given above.

As one can see from Table II, most LDA effective mass values are smaller than the corresponding sX-LDA values, usually within 20% or less. Two significant exceptions to this trend are the CB effective mass of monoclinic zirconia in the direction $\Gamma \rightarrow B$, where the sX-LDA effective mass is a factor of 3.5 larger, and the $\Gamma \rightarrow X$ direction in the VB of tetragonal zirconia, where the sX-LDA effective mass is a factor of 2 smaller than the corresponding LDA result. These differences have potentially important consequences for exciton dynamics.

In monoclinic zirconia, the lowest electron and hole effective masses are in the [100] and [001] directions, respectively, Table II. However, the corresponding hole and electron effective masses are factors of 5–10 times larger. As a result, there is only one crystallographic direction in this phase, the [010], in which electrons and holes can *both* move easily. Thus, exciton motion in monoclinic zirconia is relatively restricted, and access to the network of water-filled pores near the metal-oxide interface is limited.

Conversely, the low mobility (i.e., the large effective mass) directions in tetragonal zirconia are the same for conduction band electrons as for valence band holes, cf., Table II. Hence, both carriers and excitons can move relatively freely in the perpendicular plane. For the tetragonal phase, the smallest effective masses for both an electron and a hole are in the [111] direction. Finally, as expected, cubic zirconia is more isotropic than either monoclinic or tetragonal zirconia, so that carriers can effectively move in all directions.

STRUCTURAL AND ELECTRONIC PROPERTIES

To understand the differences in the band topologies of the three zirconia phases, we analyze their structural and electronic properties. Because the conduction and valence bands in ZrO_2 are formed from the bonding-antibonding

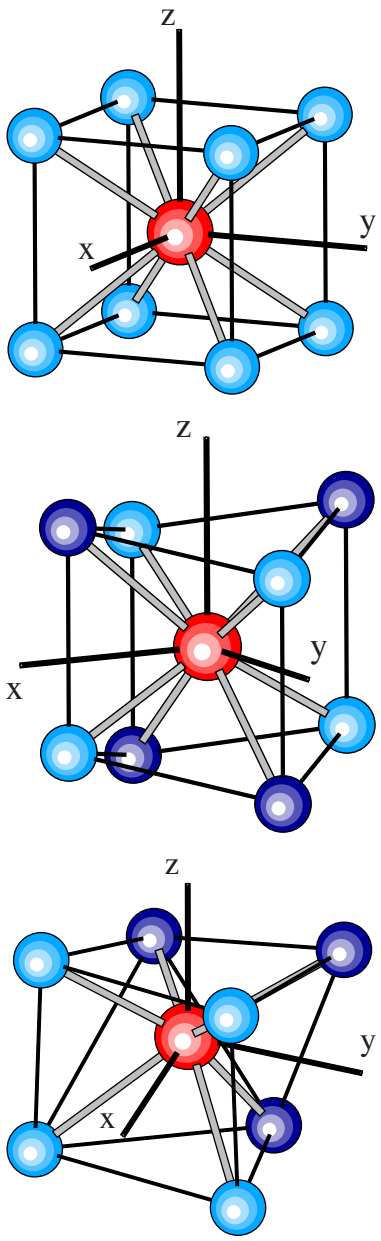

FIG. 4. (Color online) Oxygen coordination of Zr atoms in the cubic (left), tetragonal (center), and monoclinic (right) phases.

oxygen *p* and zirconium *d* states, the overlap between these spatially highly anisotropic orbitals should be very sensitive to the oxygen coordination and the distortions of the polyhedra and of the Zr-O-Zr chains. First, we note that in both the tetragonal and cubic phases, the Zr atoms have eight oxygen neighbors, while in the monoclinic phase, there are only seven O atoms around each zirconium and the oxygen coordination is strongly distorted, Fig. 4. The optimized Zr-O distances are found to be equal to 2.19 Å for the cubic, 2.07 and 2.34 Å for the tetragonal, and 2.04–2.25 Å for the monoclinic phases. Significantly, we find that in the monoclinic phase, Zr-O pairs with shorter distances ($\leqslant$2.13 Å in the range specified above) form chains running along the *y* direction. These chains are connected into a three-dimensional network via the longer Zr-O distances. Therefore, a better orbital overlap may explain the high energy dispersion along the *y* direction in monoclinic ZrO_2. Indeed, the calculated charge density distribution at the bottom of the conduction band, Fig. 5(a), or at the top of the valence band,

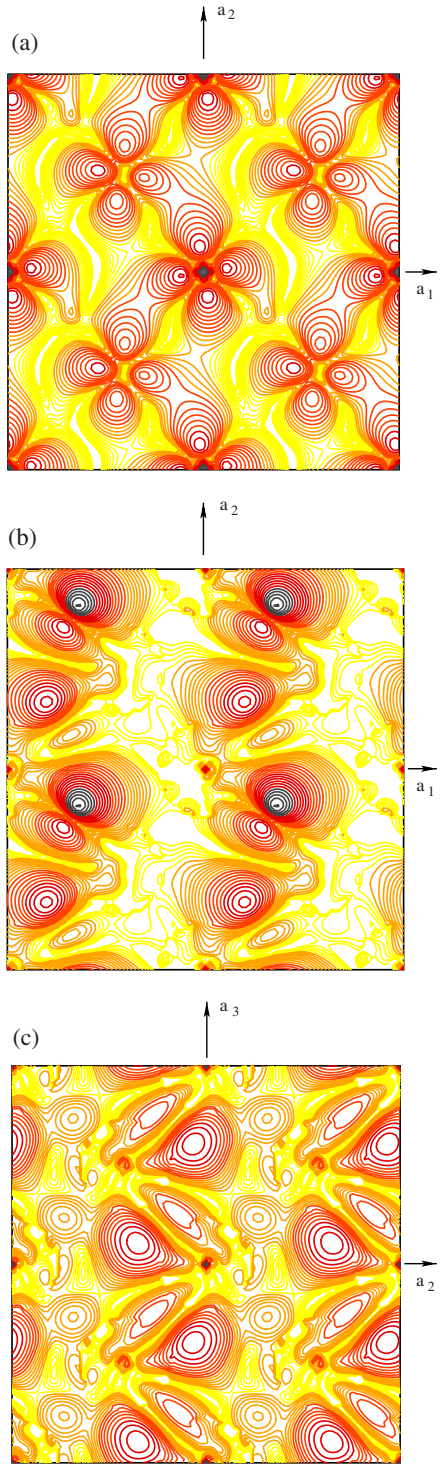

FIG. 5. (Color online) Charge density distribution calculated within a 30 meV energy range (a) above the bottom of the conduction band or [(b) and (c)] below the top of the valence band in monoclinic ZrO_2. Zr atoms are in the corners, in the center, and in the middle of the edges.

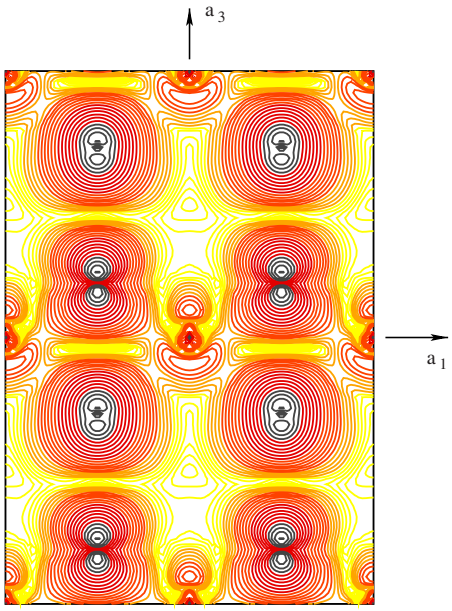

FIG. 6. (Color online) Charge density distribution calculated within a 30 meV energy range below the top of the valence band in the tetragonal ZrO_2. Zr atoms are in the corners, in the center, and in the middle of the edges.

Fig. 5(b), illustrates the chains formed from the empty x^2-y^2 orbitals of Zr and the antibonding oxygen p orbitals or mainly from the oxygen bonding p states, respectively. As discussed below, this results in the low effective mass in the [010] direction for both the electrons and holes in the low-symmetry monoclinic phase.

Because in both tetragonal and monoclinic ZrO_2 the Zr x^2-y^2 orbitals form the bottom of the conduction band, the interactions along the z direction are weak. Therefore, the electron effective masses are largest in the [001] direction for both phases, Table II. Note that the LDA gives similar values of the effective masses along this direction for the tetragonal and monoclinic phases, while the screened exchange affects only the monoclinic zirconia and triples the corresponding LDA value, Table II. We analyze the contribution from the oxygen states to the conduction band wave function and find that it is decreased by 23% in the monoclinic and by 9% in the tetragonal phases when the nonlocal corrections to the LDA are taken into account. Thus, screened exchange reduces the p-d interaction resulting in the pronounced increase of the electron effective mass in the [001] direction for monoclinic zirconia.

The top of the valence band in the tetragonal phase is formed by the bonding oxygen p and Zr $3z^2-r^2$ orbitals. Because there is no oxygen atom above or below the Zr atom in the z direction, the interaction is weak along this direction (cf. Fig. 6). As a result, the hole effective mass is large in the [001] direction, (cf. Table II). In the monoclinic phase, we find that due to the strong structural distortions, the oxygen p orbitals overlap along the y and z directions but not along the x direction: Figs. 5(b) and 5(c) illustrate anisotropic and relatively uniform charge density distributions in the xy and yz planes, respectively. Hence, the hole effective mass is significantly larger in the [100] direction for this low-symmetry phase.

SUMMARY

In conclusion, accurate first-principles band structure investigations of the monoclinic, tetragonal, and cubic zirconia phases were performed using LDA and sX-LDA approaches. The screened-exchange extension of the local density approximation predicts the largest indirect band gap in the monoclinic phase, i.e., the phase order of the indirect band gaps is $m>t>c$, which is different from the LDA result $t>m>c$. The calculated sX-LDA zero-temperature fundamental band gaps are above the LDA values by 2.0–2.5 eV and for all three phases range from 5.9 to 6.1 eV. Most significantly, we found that the conduction and valence band topologies of monoclinic zirconia are highly anisotropic with the sX-LDA electron and hole effective masses varying by factors of 5 and 10, respectively. Thus, in striking contrast to the tetragonal and cubic zirconia phases, the conduction band electrons and valence band holes in the monoclinic phase move primarily in perpendicular planes, (100) and (001), respectively, so that exciton motion is limited to a single crystallographic direction, [010].

The results reported herein may be relevant in explaining recent experimental observations suggesting that exciton production via gamma radiation in zirconia crystallites immersed in water is responsible for the accelerated dissociation of adsorbed water molecules on crystalline surfaces and for the specificity of the effect to the tetragonal zirconia phase. Furthermore, the enhanced dissociation of water on tetragonal zirconia may have important implications for understanding the acceleration in Zircaloy corrosion kinetics under irradiation.

ACKNOWLEDGMENT

Work at Northwestern is supported through the NSF NU MRSEC (Grant No. DMR-0076097/006).

*juliaem@mst.edu

[1] A. Yilmazbayhan, A. T. Motta, R. J. Cornstock, G. P. Sabol, B. Lai, and Z. Cai, J. Nucl. Mater. **324**, 6 (2004).
[2] B. Cox and A. Donner, J. Nucl. Mater. **47**, 72 (1973).
[3] J. S. Bryner, J. Nucl. Mater. **82**, 84 (1979).
[4] A. W. Urquhart, D. A. Vermilyea, and W. A. Rocco, J. Electrochem. Soc. **125**, 199 (1978).
[5] F. Garzarolli, H. Seidel, R. Tricot, and J. P. Gros, Zirconium in the Nuclear Industry: Ninth International Symposium, Kobe, Japan, 1990, edited by C. M. Eucken and A. M. Garde [ASTM Spec.

Tech. Publ. **132**, 395 (1991)].
[6] D. Pacheur, J. Godlewski, P. Billot, and J. Thomazet, Zirconium in the Nuclear Industry: Eleventh International Symposium, Garmisch-Partenkirchen, Germany, 1995, edited by E. R. Bradley and G. P. Sabol [ASTM Spec. Tech. Publ. **1295**, 94 (1996)].
[7] S. Abolhassani, R. Restani, T. Rebac, F. Groeschel, W. Hoffelner, G. Bart, W. Goll, and F. Aeschbach, J. ASTM Int. **2**, 467 (2005).
[8] X. Iltis, F. Lefebvre, and C. Lemaignan, J. Nucl. Mater. **224**, 1109 (1995).
[9] J. Godlewski, J. P. Gros, M. Lambertin, J. F. Wadier, and H. Weidinger, Zirconium in the Nuclear Industry: Ninth International Symposium, Kobe, Japan, 1990, edited by C. M Eucken and A. M. Garde [ASTM Spec. Tech. Publ. **1132**, 416 (1991)].
[10] J. Godlewski, P. Bouvier, G. Lucazeau, and L. Fayette, Zirconium in the Nuclear Industry: Twelfth International Symposium, Toronto, Canada, 1998, edited by G. P. Sabol and G. D. Moran [ASTM Spec. Tech. Publ. 11354, 877 (2000)].
[11] N. G. Petrik, A. B. Alexandrov, and A. I. Vall, J. Phys. Chem. B **105**, 5935 (2001).
[12] J. A. LaVerne, J. Phys. Chem. B **109**, 5395 (2005).
[13] H. J. F. Jansen and J. A. Gardner, Physica B & C **150**, 10 (1988).
[14] F. Zandiehnadem, R. A. Murray, and W. Y. Ching, Physica B & C **150**, 19 (1988).
[15] N. I. Medvedeva, V. P. Zhukov, M. Ya. Khodos, and V. A. Gubanov, Phys. Status Solidi B **160**, 517 (1990); V. A. Gubanov and N. I. Medvedeva, Physica B **172**, 285 (1991).
[16] H. J. F. Jansen, Phys. Rev. B **43**, 7267 (1991).
[17] R. H. French, S. J. Glass, F. S. Ohuchi, Y. N. Xu, and W. Y. Ching, Phys. Rev. B **49**, 5133 (1994).
[18] D. W. McComb, Phys. Rev. B **54**, 7094 (1996).
[19] B. Kralik, E. K. Chang, and S. G. Louie, Phys. Rev. B **57**, 7027 (1998).
[20] J. K. Dewhurst and J. E. Lowther, Phys. Rev. B **57**, 741 (1998); J. E. Lowther, J. K. Dewhurst, J. M. Leger, and J. Haines, Phys. Rev. B **60**, 14485 (1999).
[21] G. Jomard, T. Petit, A. Pasturel, L. Magaud, G. Kresse, and J. Hafner, Phys. Rev. B **59**, 4044 (1999).
[22] L. K. Dash, N. Vast, P. Baranek, M.-C. Cheynet, and L. Reining, Phys. Rev. B **70**, 245116 (2004).
[23] E. Wimmer, H. Krakauer, M. Weinert, and A. J. Freeman, Phys. Rev. B **24**, 864 (1981); M. Weinert, E. Wimmer, and A. J. Freeman, *ibid.* **26**, 4571 (1982).
[24] D. M. Bylander and L. Kleinman, Phys. Rev. B **41**, 7868 (1990).
[25] A. Seidl, A. Görling, P. Vogl, J. A. Majewski, and M. Levy, Phys. Rev. B **53**, 3764 (1996).
[26] W. Wolf, E. Wimmer, S. Massidda, M. Posternak, and C. B. Geller, Am. Phys. Soc. March Meeting, Los Angeles, CA, 1998, edited by B. H. Ripin [Bull. Am. Phys. Soc. 43, 797 (1998)].
[27] R. Asahi, W. Mannstadt, and A. J. Freeman, Phys. Rev. B **59**, 7486 (1999).
[28] M. Y. Kim, R. Asahi, and A. J. Freeman, J. Comput.-Aided Mater. Des. **9**, 173 (2002).
[29] C. B. Geller, W. Wolf, S. Picozzi, A. Continenza, R. Asahi, W. Mannstadt, A. J. Freeman, and E. Wimmer, Appl. Phys. Lett. **79**, 368 (2001).
[30] M. Y. Kim, Y. J. Zhao, A. J. Freeman, and W. Mannstadt, Appl. Phys. Lett. **84**, 3579 (2004).
[31] S. Jin, Y. Yang, J. E. Medvedeva, J. R. Ireland, A. W. Metz, J. Ni, C. R. Kannewurf, A. J. Freeman, and T. J. Marks, J. Am. Chem. Soc. **126**, 13787 (2004).
[32] M. Kim, A. J. Freeman, and C. B. Geller, Phys. Rev. B **72**, 035205 (2005).
[33] J. E. Medvedeva, A. J. Freeman, X. Y. Cui, C. Stampfl, and N. Newman, Phys. Rev. Lett. **94**, 146602 (2005).
[34] S. H. Rhim, M. Kim, A. J. Freeman, and R. Asahi, Phys. Rev. B **71**, 045202 (2005).
[35] A. H. MacDonald, W. E. Pickett, and D. D. Koelling, J. Phys. C **13**, 2675 (1980).
[36] R. S. Sokolova, Sov. J. Appl. Phys. **41**, 454 (1974).
[37] J. Frandon, B. Brouseau, and F. Pradal, Phys. Status Solidi B **98**, 379 (1980).
[38] C.-K. Kwok and C. R. Aita, J. Appl. Phys. **66**, 2756 (1989).
[39] E. Elizalde, J. M. Sanz, F. Yubero, and L. Galan, Surf. Interface Anal. **16**, 213 (1990).
[40] As obtained from additional calculations for monoclinic ZrO_2 with a background charge added to model the degenerate *n* or *p* doping.